Völlenkle. Thanks are due also to the Centro di Cristallografia Strutturale del CNR di Pavia for recording the counter data of sample (IV). All calculations were carried out at the Centro di Calcolo dell'Università di Modena.

References

ALBERTI, A. (1972). *Tschermaks Mineral. Petrogr. Mitt.* **18**, 129–146.
ALBERTI, A. (1973). *Tschermaks Mineral. Petrogr. Mitt.* **19**, 173–184.
ALBERTI, A. (1975). *Tschermaks Mineral. Petrogr. Mitt.* **22**, 25–37.
ALIETTI, A., GOTTARDI, G. & POPPI, L. (1974). *Tschermaks Mineral. Petrogr. Mitt.* **21**, 291–298.
BARTL, H. (1973). *Z. Kristallogr.* **137**, 440–441.
BRESCIANI-PAHOR, N., CALLIGARIS, M., NARDIN, G. & RANDACCIO, L. (1981). *J. Chem. Soc. Dalton Trans.* pp. 2288–2291.
BRESCIANI-PAHOR, N., CALLIGARIS, M., NARDIN, G., RANDACCIO, L. & RUSSO, E. (1980). *J. Chem. Soc. Dalton Trans.* pp. 1511–1514.
BUSING, W. R., MARTIN, K. O. & LEVY, H. A. (1962). *ORFLS.* Report ORNL-TM-305. Oak Ridge National Laboratory, Tennessee.
HAJDÚ, F. (1972). *Acta Cryst.* A**28**, 250–252.
HANSON, H. P., HERMAN, F., LEA, J. D. & SKILLMAN, G. (1964). *Acta Cryst.* **17**, 1040–1044.
KOYAMA, K. & TAKÉUCHI, Y. (1977). *Z. Kristallogr.* **145**, 216–239.
MERKLE, A. B. & SLAUGHTER, M. (1968). *Am. Mineral.* **53**, 1120–1138.
PASSAGLIA, E., PONGILUPPI, D. & VEZZALINI, G. (1978). *Neues Jahrb. Mineral. Monatsh.* pp. 310–324.

Acta Cryst. (1983). B**39**, 197–209

A Transmission Electron Microscopical Study of the σ Phase in an Iron–Chromium Steel

BY P. G. SELF*

Department of Metallurgy and Materials Science, University of Cambridge, Cambridge, England

M. A. O'KEEFE

High Resolution Electron Microscope, Free School Lane, University of Cambridge, Cambridge, England

AND W. M. STOBBS

Department of Metallurgy and Materials Science, University of Cambridge, Cambridge, England

(*Received* 20 *October* 1981; *accepted* 19 *October* 1982)

Abstract

This paper details several aspects of the σ phase in a duplex stainless steel. The growth and morphology of the phase is characterized and it is demonstrated that under certain conditions the nature of the nucleation and growth produces faulting within the σ-phase particles. The crystalline structure of the phase is discussed with reference to the possibility that it might be that of β-uranium rather than that previously reported. In this connection a comparison is made of the relative usefulness of high resolution and various indirect methods for analysing the structure. In particular, the absences in diffraction patterns and their dependence on crystal tilt and thickness offer an insight into the requirements for accurate structure determination by high-resolution electron microscopy. Finally, the fault structure is examined and a planar (110)-type fault is discussed in detail.

1. Introduction

The σ phase arises in a number of binary and also ternary transition-metal alloy systems. It is of interest technologically in that its formation in high-alloy steels, based on the Fe–Cr system, tends to lead to embrittlement. This is essentially because, once nucleated, σ-phase particles can grow to relatively large sizes and are particularly hard; the sequence faults they typically contain not being easily sheared. The phase is of

* Presently at Department of Geology, Arizona State University, Tempe, Arizona, USA.

0567-7408/83/020197-13$01.50

theoretical interest in the general field of alloy formation in that its formation is complex and apparently a function of both the relative atomic radii of its constituent atoms and the number of electron vacancies in their valence shells. The effect of alloying elements is, for example, interpreted in terms of the exchange of valence electrons. The reader is referred to both the review by Hall & Algie (1960) and *The Theory of Alloy Phases* (Kasper, 1956) for general discussion of both the mechanical and structural properties of the σ phase.

A detailed knowledge of the structure of the σ phase is clearly useful in interpreting its formation whilst a classification of the defect structures that it can contain is essential in clarifying the way in which it can embrittle the alloy in which it is formed. In the investigation described in this paper a variety of electron microscopical techniques have been used to study the mode of growth (§3), structure (§4) and defect form (§5) of σ particles in an Fe–Cr-based duplex stainless steel.

2. The alloy investigated and experimental methods

The composition of the steel used in this study was nominally: 26 wt%Cr, 5 wt%Ni, 1·3 wt%Mo and 0·3 wt%C with the balance Fe. In the Fe–Cr binary system the σ phase forms with a composition in the range 40 to 50 wt% chromium at temperatures between 823 and 1088 K. σ formation takes over from the so-called 748 K embrittlement process in which α′ (chromium-rich Guinier–Preston zones) forms. This suggests that σ formation involves long-range diffusion of chromium. Extra alloying elements have, however, varied effects on the formation process. For example, in Fe–Cr, concentrations of aluminium above 1·25 wt% are known to suppress σ formation completely. In this study the alloying elements of interest are nickel and molybdenum. The latter markedly increases the $(Fe–Cr)_\sigma$ phase field while in Fe–Cr–Ni alloys the σ field does not extend above 5 wt%Ni.

Electron-microscope specimens containing σ-phase particles were prepared from homogenized steel rods of 3 mm diameter which, after a 5 min anneal at 1573 K followed by a water quench, were cold-rolled to a thickness of about 0·3 mm. For the work described in §3 the rolled alloy was given a further recrystallization treatment at 1573 K for 5 min again followed by water quenching. Otherwise discs of 2·3 mm diameter were punched directly from the cold-rolled alloy and annealed at 1023 K whilst sealed in quartz tubes under a partial pressure of argon for times ranging from 5 min to 3 h before a final water quench. Annealing times of this order were quite adequate for the formation of a relatively high volume fraction of large σ particles. The annealed discs were mechanically lapped to a thickness of 0·1 mm before being electropolished for examination in the transmission electron microscope using a twin-jet system. The electropolishing solution used was 2·5 vol.% perchloric acid in methanol cooled to 238 K, the voltage applied being 45–55 V. It was found that foils could be adequately polished at room temperature in the above solution but at the lower temperature the σ phase and the matrix polished at more or less the same rate giving little difference in the specimen thickness across a σ–matrix boundary.

While a JEOL 200A and a Philips 400T were used for the general investigation, the high-resolution work was done using a JEOL 120CX with a 0·7 mm C_s objective lens.

3. σ-phase growth and morphology

As the σ phase significantly degrades the properties of steels, much work has been carried out on its nucleation and growth; mainly with the aim of retarding its formation. It is generally accepted that the growth of σ proceeds sluggishly but in fact it can form rapidly given suitable nucleating sites. This indicates that nucleation is the slow step in the precipitation of the σ phase.

Examination of the ternary phase diagram for the Fe–Ni–Cr system shows that the alloy used lies on the boundary of the σ-phase field. For the annealing treatment given the nucleation of σ is preceded by the formation of austenite and the carbide $M_{23}C_6$ (Southwick, 1978). The effect of the growth of austenite (γ) is to deplete the ferrite (α) matrix of nickel and enrich it with chromium (Southwick & Honeycombe, 1980). This, together with the effect of molybdenum in broadening the σ-phase field, facilitates the nucleation of σ. A typical region of the cold-rolled

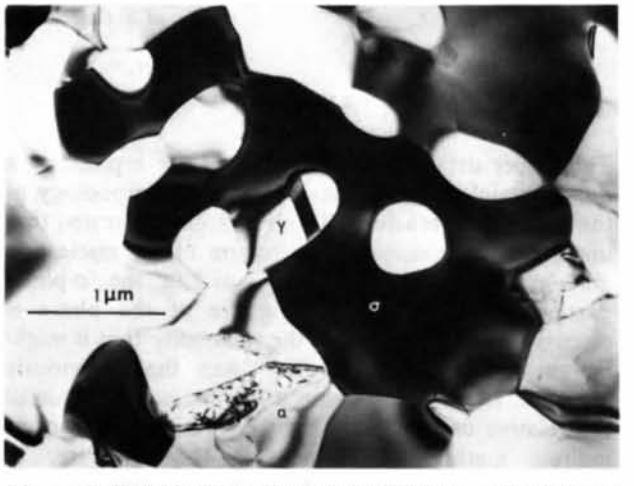

Fig. 1. Bright-field micrograph of cold-rolled and annealed (1023 K) alloy showing α, γ and σ intergrowth. σ, as here, is generally easy to identify because of its high scattering power and large unit-cell size.

alloy after annealing at 1023 K for 30 min is shown in Fig. 1. The micrograph demonstrates the severe intergrowth of α, γ and σ in the alloy. The σ apparently nucleates on defects and rapidly grows along them forming honeycomb-shaped crystals. The defects play the dual role of facilitating nucleation and acting as diffusion paths for chromium.

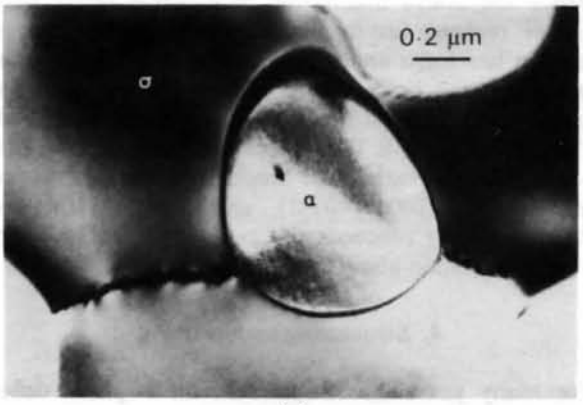

(*a*)

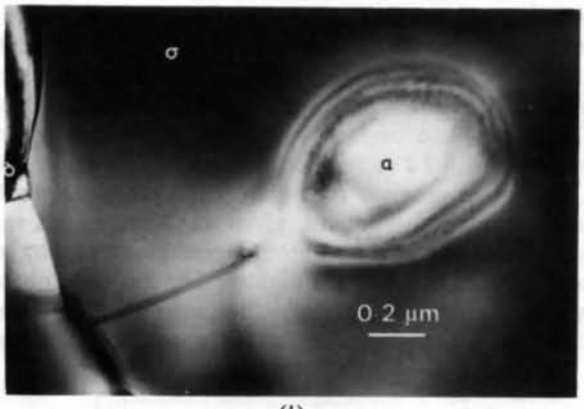

(*b*)

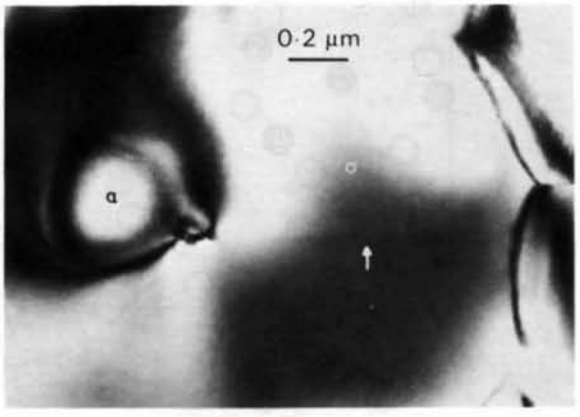

(*c*)

Fig. 2. Bright-field micrographs of cold-rolled and annealed (1023 K) alloy. The figures demonstrate the tendency to form faults joining the entrapped ferrite with ferrite on the outside of the honeycomb-shaped σ particles. Note that in (*a*) the fault is associated with high-strain-field defects which tend to anneal out as σ growth proceeds [*cf.* 2(*b*)].

In the cold-rolled alloy, the rapid growth along defects causes the σ to close off around regions of α matrix. When the σ does this it tends to leave a string of defects along the join (Fig. 2*a*). As the σ continues to grow, these defects anneal finally forming planar faults [of sequence type (see §5)] running right through the σ to the entrapped α (Figs. 2*b* and *c*). The retained α particles may either rotate or even shear as they are further transformed (Fig. 3). If the entrapped α is to transform to σ completely there must be some diffusion of chromium through the σ to the α and this presumably is achieved along the faults formed as described above. Should these faults anneal completely out of the σ, the chromium diffusion rate will be severely retarded and the transformation of the entrapped α all but stops. It is this which leads to the honeycomb morphology generally seen.

In dual-phase steels the σ phase does not necessarily only form at defects and grain boundaries in the α, but is also found to nucleate at the α–γ interface. The atomic structure of the $(001)_\sigma$ face of a σ particle is essentially hexagonally close packed and so nucleation might be expected to occur with $(111)_\gamma \| (001)_\sigma$ and

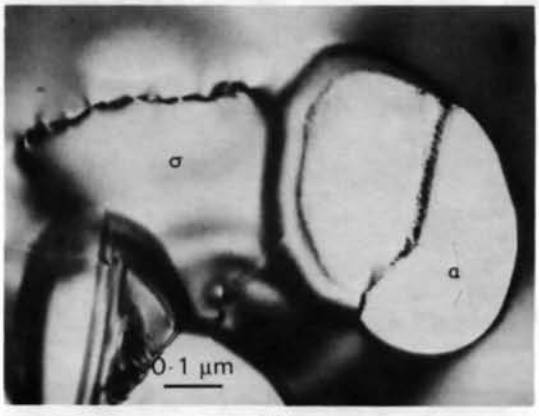

(*a*)

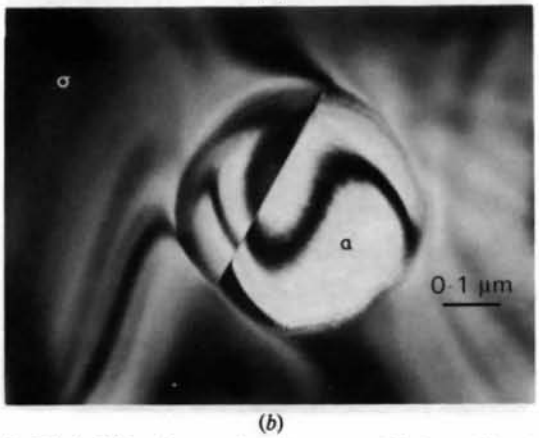

(*b*)

Fig. 3. Bright-field micrographs of entrapped ferrite which shows evidence of deformation as a result of the growth of the surrounding σ particle.

$[\bar{1}10]_\gamma \| [\bar{1}10]_\sigma$. Even if the nucleation takes place at the α/γ interface the σ particles grow wholly within the α to produce the structures as shown in Fig. 1. As the α and γ have a Kurdjumov–Sachs (K–S) orientation relationship to each other the above σ–γ orientation relationship would also specify the σ–α relation. In fully austenitic steels (and also nickel-based superalloys) the σ does in fact grow with the above orientation relationship but usually in the form of thin plates (Lewis, 1966). In the present study, σ crystals with this same orientation relationship were found in both the cold-rolled and recrystallized alloy but the occurrence of such crystals was rare. The majority of σ particles were presumably thus nucleated incoherently at grain boundaries or on defects away from α/γ boundaries.

In the recrystallized alloy the formation of σ is roughly ten times slower than in the cold-rolled material for a given ageing temperature. An orientation relationship found in the recrystallized alloy was $[110]_\sigma \| [110]_\alpha$ and $(001)_\sigma$ approximately parallel to $(1\bar{1}7)_\alpha$ (Fig. 4). Hence, although the (110) planes of the σ and α are aligned the match is by no means a simple one. Holden (1952) has discussed slip on (110) planes in β-uranium, which we will see in §4 has a closely related structure to that of the σ phase. Holden describes these planes as being 'relatively close packed'. Hence the above orientation relationship might have similar reasons for its occurrence as the K–S type relation has for α and γ. By viewing the $(110)_\sigma$ planes (see §5) it can be seen that matching of σ to α is not easy but a partial match can be obtained with $(001)_\sigma \| (001)_\alpha$. It is thus speculated that in the initial stages of this variant of nucleation the orientation relationship is $(001)_\sigma \| (001)_\alpha$ and $[110]_\sigma \| [110]_\alpha$ and that as growth proceeds the two phases rotate away from this relation about their mutual [110] axis.

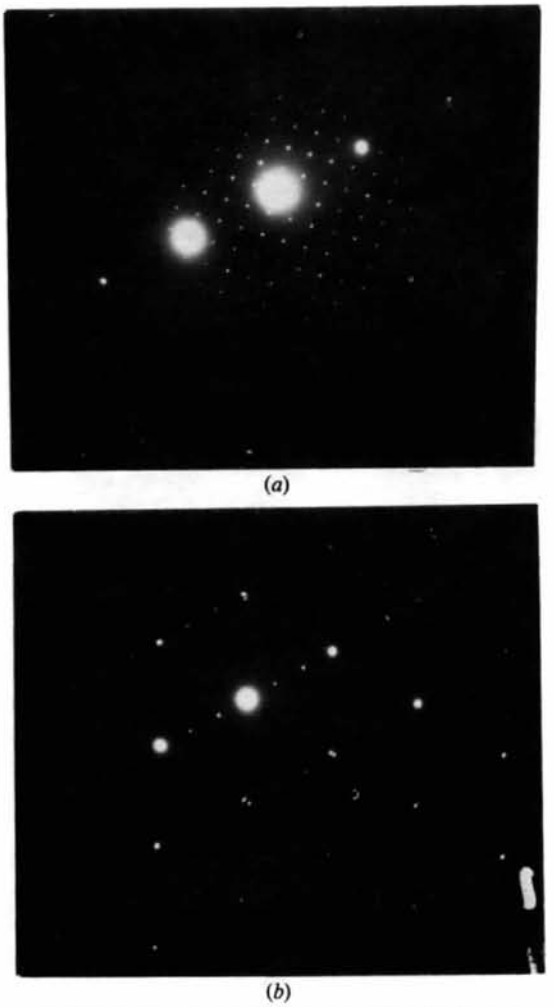

Fig. 4. (*a*) Diffraction pattern of σ particle and adjacent α matrix showing the parallelity of $[110]_\alpha$ with $[110]_\sigma$. (*b*) Diffraction pattern of the same particle tilted about $[110]_\alpha$ at $(111)_\alpha$.

4. Structuring and ordering

For many years the structure of the σ phase defied characterization. This was mainly because of the difficulty of preparing suitable specimens for X-ray studies. Then in 1954 several authors [see Hall & Algie (1966) for a review] published experimental evidence that the structure was that proposed by Duwez & Baen (1951). In this model σ is assigned a tetragonal structure with 30 atoms per unit cell, as shown in Fig. 5. The space group is $P4_2/mnm$–D_{4h}^{14} with the approximate atomic coordinates given in Table 1. X-ray studies suggest that the atomic positions vary by at most 2% from these coordinates. The Fe–Cr σ-phase system was characterized by Bergman & Shoemaker (1954) who proved the important point that the atoms

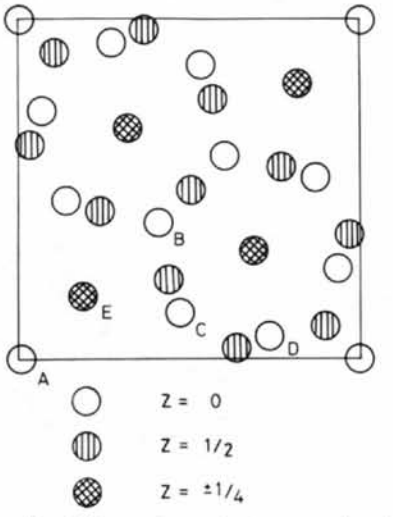

Fig. 5. Schematic of the σ-phase structure as viewed in (001). The labels identify the sites with different occupations as in Table 1. Note that the *E* sites are drawn as relaxed after Kagomé tiling-net superposition so that they lie in columns parallel to [001].

Table 1. *Atomic coordinates of σ phase*

Space group: $P4_2/mnm$–D_{4h}^{14}

Size	Type	Positions	
A	2(*a*)	$0,0,0,;\frac{1}{2},\frac{1}{2},\frac{1}{2}$	
B	4(*f*)	$x_b, x_b, 0$	$x_b = 2/5$
C	8(*i*)	$x_c, y_c, 0$	$x_c = 7/15, y_c = 2/15$
D	8(*i*)	$x_d, y_d, 0$	$x_d = 11/15, y_d = 1/15$
E	8(*j*)	x_e, x_e, z_e	$x_e = 11/60, z_e = 1/4$

at the sites labelled *E* are situated between the layers formed in the [001] direction by the atoms at the other sites. The unit-cell dimensions were determined to be $a = 8{\cdot}800$ and $c = 4{\cdot}544$ Å.

Frank & Kasper (1959) described the structure, in terms of 'Kagomé tiling nets', as essentially consisting of alternating layers of close-packed atoms (stacking along the *c* axis) rotated by 90° to each other. For complete specification of the structure (as described above) in this way a slight distortion (approx. 4%) from the true hexagonal structure is required. A further distortion is necessary at the *E* sites [apart from the displacement by $\frac{1}{4}$ (001) out of the plane] to allow the atoms there to lie, supposedly, in straight columns at the position determined by the average of the sites predicted by the two rotated close-packed nets. The structure has been generally described as being topologically close packed because it contains only tetrahedral interstices. This allows it to fill space efficiently with spheres of slightly different radius.

Although the structure has a relatively large unit-cell, the 001-zone kinematical diffraction pattern is fairly open. The first strong reflections are the 410, 330 and related reflections. These are the first-order reflections of the two hexagonal nets which describe the structure. Other reflections in the pattern are weak and their presence is due to atomic ordering and to imperfect atomic-site positions relative to the nets. 100 kV convergent-beam electron diffraction patterns of $(Fe–Cr)_\sigma$ obtained at 001, $1\bar{1}0$ and 101 are shown in Figs. 6(*a*), (*b*) and (*c*), respectively. Considering firstly the 001 diffraction pattern it is clear that multiple scattering has caused the majority of the kinematically disallowed diffraction spots to have some intensity. The only dynamically forbidden reflections are the *h*00 for *h* odd and 0*k*0 for *k* odd.

A particularly interesting feature of the 001 diffraction pattern is the irregular dark ring running through the 200, 210 and related reflections. This ring occurs at all crystal thicknesses (the diffraction pattern being obtained from an area with a broad range of thicknesses) but only when the crystal is oriented very close to the (001) normal. Unlike the characteristic dark lines through, for example, the 0*k*0 for *k* odd reflections in the 101 pattern in Fig. 6(*c*), the absences of intensity in the dark ring in the 001 pattern would

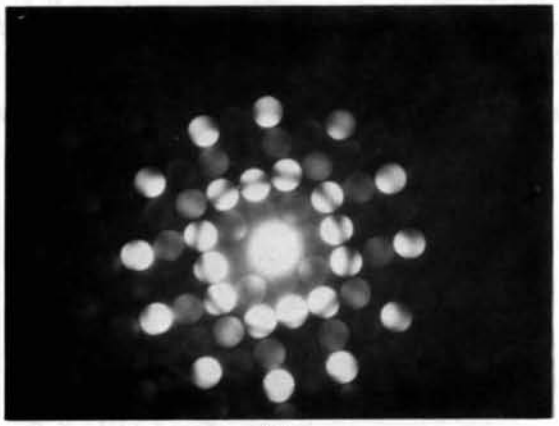

(*a*)

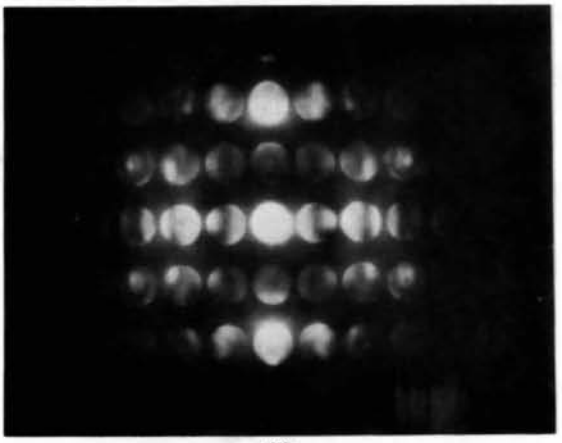

(*b*)

Fig. 6. (*a*) Convergent-beam (divergence ~2·5 μrad) diffraction pattern showing 001_σ. The first strong kinematically allowed reflections lie in the 410 and 330 rings. Note particularly the dark band bassing through the 200 and 210 type reflections. (*b*) Convergent-beam diffraction pattern showing $1\bar{1}0_\sigma$. 00*l* is vertical.

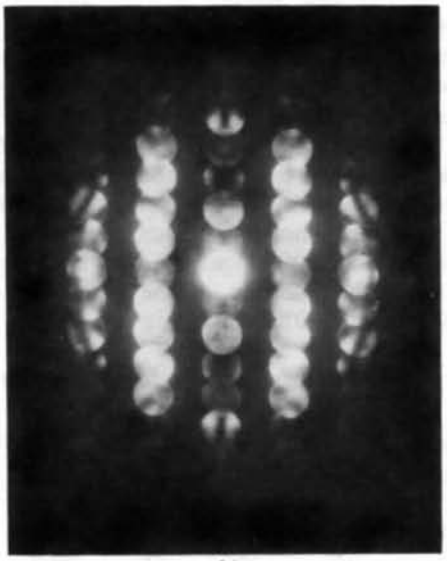

(*c*)

Fig. 6 (*cont.*) (*c*) Convergent-beam diffraction pattern showing 101_σ. 0*k*0 is vertical.

not appear to be interpretable in terms of extra symmetries in the structure. This is because they are only present along a small segment of the line which would indicate an extra symmetry as introduced by a glide or screw axis (Gjønnes & Moodie, 1965). Furthermore, it is unlikely that the effect can be attributed to upper-Laue-line interactions because of both the large angles and width of the band and the large distance between the zero-order plane and the upper Laue zones which contain the reflections directly above and below the 200, 210 and related reflections. (The first are the 202, 212, *etc.*)

As mentioned above the 200 and 210 reflections are kinematically weak; however, they both have a double diffraction path from a 140 reflection and either a $1\bar{4}0$ or $3\bar{3}0$ type reflection, all of which are kinematically strong. This suggests that the forbidden ring could be due to a balancing of the kinematical intensity with that due to multiple scattering from the strong reflections. The kinematical intensity of the 200 and 210 spots is dependent on the ordering of the alloy.

Much work has been done on the atomic ordering of the σ phase. The ordering schemes considered in this paper are given in Table 2. The schemes OR2 and OR3 are suggested by the work of Bergman & Shoemaker (1954); the first by their work directly on $(Fe–Cr)_\sigma$ and the second inferred from their $(Fe–Mo)_\sigma$ results. OR4 is from Kasper (1956) and OR5 is the generalized ordering scheme derived from a study of all σ phases.

To investigate the effect of ordering on diffracted intensities and to see if the dark ring is predictable, dynamical intensities were computed by the multislice method using 441 beams out to $|hkl| = |17,17,0|$. As any experimental diffraction pattern is an average over some range of thickness it was found more instructive to display thickness fringes as a function of tilt. The resulting theoretical thickness fringes for the 210 beam for some of the ordering schemes are shown in Fig. 7. The beam tilts used are indicated in Fig. 7(*d*) by their corresponding point on a 001 convergent-beam pattern. It can be seen that the resulting fringes vary little from ordering scheme to ordering scheme (this is also true for those not shown). The results for the 200 thickness fringes were very similar (as is expected from the fact that the 210 and 200 beams are very closely related). Fig. 7(*c*) is the intensity of the 210 beam for the ordering scheme OR2 including the effect of out-of-zone reflections. This was calculated in the standard way (Lynch, 1971) using four different slices per unit cell parallel to the beam direction. In this case, as well as in those not shown, the out-of-zone relections have little effect on the diffraction intensities. Fig. 7(*c*) does not of course include the effects of the reflections in the upper layers near to the Ewald sphere. If, however, reflections in the first high-order-Laue-zone ring were important in explaining the dark ring then the effect would be sensitive to accelerating voltage which it is not: the dark ring can be seen at 100 and 120 kV. Standard multislice calculations of the type we have used can be modified in a number of ways when attempting to match intensities carefully. A lack of sphericity for the atomic potentials might be included and the Debye–Waller factors need not be assumed to be isotropic. It is, however, clear that there is a *gross* discrepancy between the behaviour predicted on tilting and that observed: at none of the orientations do any of the predicted fringes show a thickness-*independent* minimum near to the symmetrical orientation. It would thus seem reasonable to conclude that the forbidden ring is not due to ordering alone.

The main multiple scattering to a 200 reflection at the (001) normal is via $1\bar{4}0 + 140$ or $140 + 1\bar{4}0$ given

Table 2. *Ordering schemes for σ phase*

Ordering scheme	Site and occupancy				
	A	*B*	*C*	*D*	*E*
OR1	Mixed	Mixed	Mixed	Mixed	Mixed
OR2	Fe	Cr	Mixed	Mixed	Cr
OR3	Fe	Cr	Fe	Mixed	Mixed
OR4	Fe	Cr	Mixed	Fe	Cr
OR5	Fe	Cr	Mixed	Fe	Mixed
OR6	Fe	Cr	Cr	Fe	Mixed

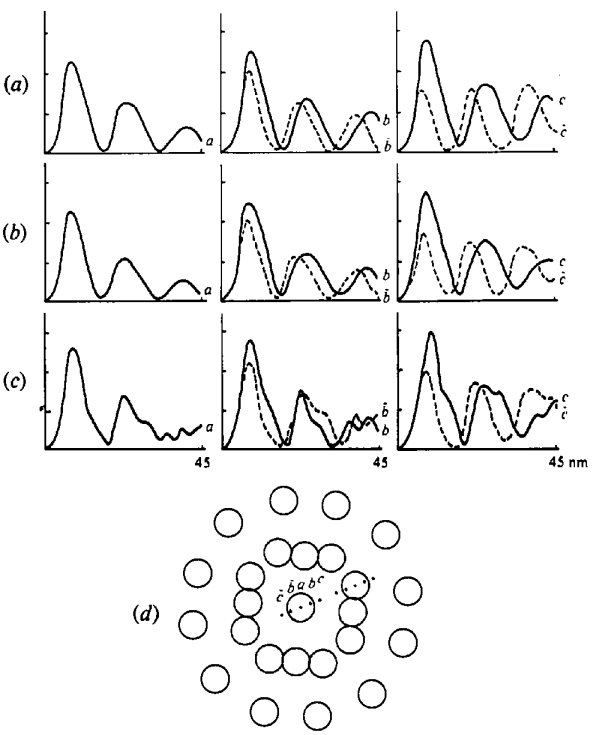

Fig. 7. Theoretical thickness profiles for the 210 reflections at the orientations *a*, *b*, $\bar{b}$, *c* and $\bar{c}$ as marked in Fig. 8 for the ordering schemes (*a*) OR1 and (*b*) OR2. Fig. 7(*c*) is also for OR2 but with the inclusion of the effect of upper Laue zones. (*d*) Schematic of a 001 zone convergent-beam pattern. The positions *a*, *b*, $\bar{b}$, *c* and $\bar{c}$ indicate the beam tilts used in the intensity calculations shown in (*a*), (*b*), (*c*) and Fig. 9.

that these are the first strong reflections. We have investigated the strong contribution of multiple diffraction to the 200 and 210 reflections by the above and other routes by comparing the amplitudes and phases in these beams for multislice calculations using only 37 beams (out to 0·4 Å^{-1}, *i.e.* excluding the 410 and 330 reflections) both with a full calculation employing 973 beams and with one in which $V(330)$ and $V(140)$ were artificially set to zero. The amplitudes for the 210 beam for these three calculations are compared in Figs. 8(*a*), (*b*) and (*c*). It can be seen both that the predominant double diffraction path in this case is, as we expected, that involving 330 and 140 reflections and that, given the rapid variation with thickness of both the amplitudes and phases of the strong dynamical contribution to 210, the relative independence of the dark ring to thickness is not due to cancellations of the kinematic 210 amplitude by double scattering.

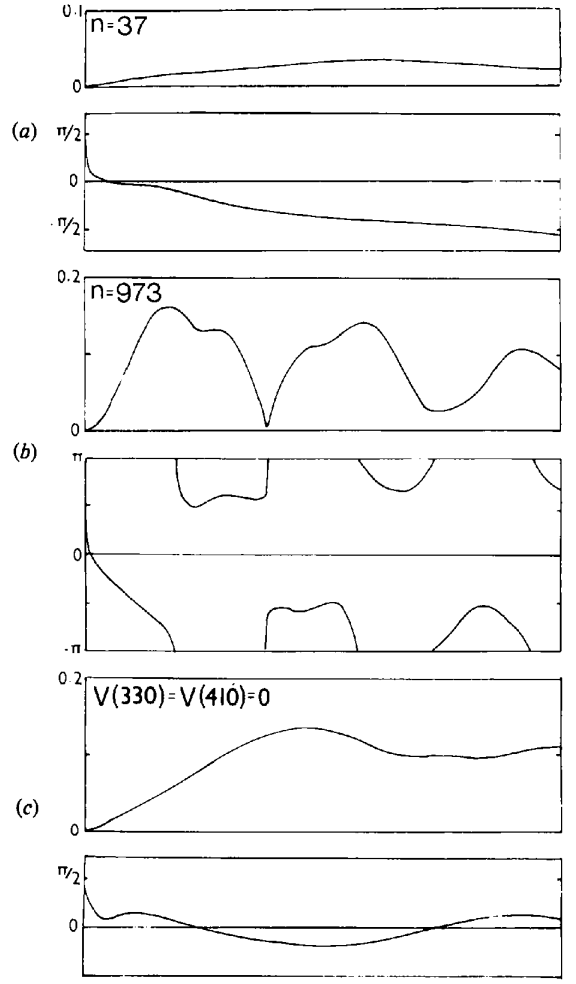

Fig. 8. The changes in amplitude and phase, with thickness, of the 201 beam (*a*) for a 37-beam calculation, (*b*) for a full 973-beam calculation and (*c*) for V' (330) and V' (410) set equal to zero. Note the strong effects of double diffraction and the way this is markedly thickness dependent. The thickness range is 45 nm.

The predominant reason for the form of the structure factors of the 200 and 210 beams is that the atoms at the *E* sites are deemed to lie in straight columns along the [001] direction. If they were allowed to lie in the positions predicted by the overlaying of the Kagomé tiling nets the structure factors of these beams are reduced (*e.g.* to zero in the case of a solid solution) and may even be of reversed sign in certain ordering schemes (see Fig. 12). Such positioning of the *E*-sited atoms is not unreasonable as these atoms are by far the closest together. Their separation here is approximately 2·27 Å whilst the next closest set of atoms (*C*–*C* and *A*–*D*) are some 2·39 Å apart. The theoretical thickness fringes for a unit cell with atoms at the *E* sites repositioned as above and for ordering scheme OR6 are shown in Fig. 9. The encouraging feature of the predicted changes in intensity as a function of orientation is that now, as the beam is tilted away from the symmetrical position in either direction, the intensity in the beam increases to well above that at the on-zone condition. There is still some considerable variation in the intensity with thickness but this is less marked than for the unmodified structure, and is, as is demonstrated in Figs. 8(*a*), (*b*) and (*c*), principally due to double diffraction. It would thus seem reasonable to suggest that the atoms at the *E* sites in $(Fe–Cr)_\sigma$ might lie in laterally staggered vertical rows.

Further supportive evidence for this being the reason for the dark ring in the 001 diffraction pattern was obtained in real space by examination of 210 dark-field thickness fringes over a range of orientations similar to those shown in Fig. 7(*d*) and using a low beam convergence. Fig. 10 is an example of an image obtained in this way. It shows a region where the orientation changes progressively over the required range about an axis perpendicular to the edge of the foil. Fig. 11 shows microdensitometer traces of the thickness fringes for the different orientations. These show good general agreement with the behaviour predicted for the structure with staggered atomic positions at the *E* sites. Note, for example, the characteristic way in which, away from the symmetric orientation, the second and third fringes are strengthened. This is not predicted for any of the ordering schemes without *E*-site modifications (*cf.* Fig. 7).

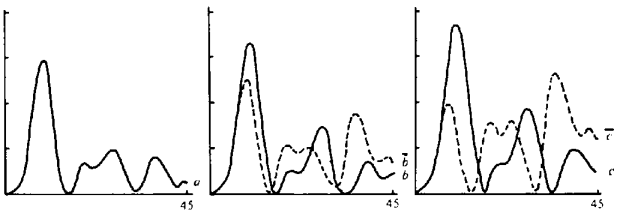

Fig. 9. Theoretical thickness profiles for the 210 reflection at the same orientations as Fig. 7 for the ordering scheme OR6 and with the *E*-sited atoms repositioned to the points predicted by the overlapping Kagomé tiling nets.

Table 3. *The maximum intensity reached by the given beams at the Laue orientation, with the beam in the* [1$\bar{1}$0] *direction, and with* 001 *and* 110 *at the Bragg orientation for the unmodified and modified structure for thickness to* 52 nm

Oriented beam		110	$\bar{1}\bar{1}0$	330	$\bar{3}\bar{3}0$	001	00$\bar{1}$	002	00$\bar{2}$
Unmodified structure	Laue: 000:	0·107	0·107	0·052	0·052	0·111	0·111	0·099	0·099
	Bragg: 001:	0·107	0·107	0·060	0·060	0·150	0·080	0·163	0·047
	Bragg: 110:	0·156	0·036	0·084	0·044	0·101	0·101	0·117	0·117
Modified structure	Laue: 000:	0·101	0·101	0·047	0·047	0·108	0·108	0·097	0·097
	Bragg: 001:	0·121	0·121	0·060	0·060	0·195	0·064	0·164	0·047
	Bragg: 110:	0·155	0·032	0·083	0·039	0·097	0·100	0·096	0·109

The modified structure above is in fact the same as that of β-uranium. Most articles on the σ phase comment on the similarities between the σ-phase structure as generally previously described with that of β-uranium, but few suggest they are identical. The difference between the two structures may be understood by comparing the space group of the conventionally accepted σ structure ($P4_2/mnm$–D_{4h}^{14}) with that of the β-uranium structure ($P4_2nm$–C_{4v}^4). D_{4h}^{14} is a subgroup of C_{4v}^4 and differs only in that the z parameters of the D_{4h}^{14} space group are set by a higher symmetry. In practice this can be lost in σ by the repositioning of the atoms at the E sites as described above. The striking difference between the two space groups is the lack of the basal-plane mirror in the 'modified' structure. Careful examination of the convergent-beam diffraction pattern in Fig. 6(*b*) at 1$\bar{1}$0 does not reveal any lack of mirror symmetry (even in the higher Laue zones) beyond that which could be due to the diffraction pattern not being quite at the (1$\bar{1}$0) normal. This does not, however, prove that the structure is not modified since it is possible that there is no inter-cell correlation between the columns of E-sited atoms. These columns are far enough apart to accommodate a random sequencing which would allow the projected average structure to retain the mirror. It is interesting that such an arrangement would lead to the potentials of the E-sited atoms being smeared out, which is possibly consistent with the fact that Bergman & Shoemaker (1954) found the E-site atom to have a lower atomic number than both Fe and Cr.

Fig. 10. Dark-field 210 image showing the edge of a σ particle with an orientation variation between b and $\bar{b}$ of Fig. 8. The convergence used in taking this micrograph was approximately 0·5 mrad.

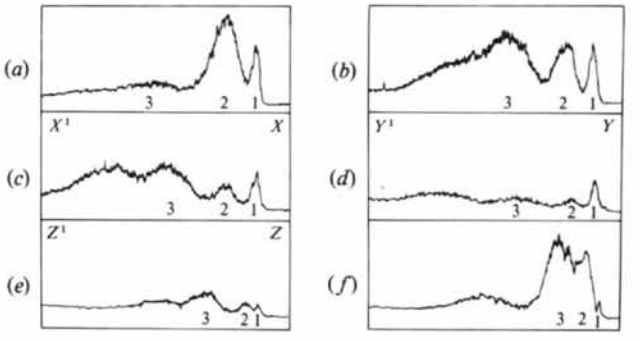

Fig. 11. Microdensitometer trace of images of thickness fringes obtained for the particle as shown in Fig. 10 for orientations between (*a*) c and (*f*) $\bar{c}$. (*c*), (*d*) and (*e*) were taken from the image shown in Fig. 10 between the indicated points.

Another feature of the 1$\bar{1}$0 convergent-beam diffraction pattern (Fig. 6*b*) is the way several of the discs show characteristic patterns of intensity variation as a function of orientation. This prompted us to investigate the effect of tilt on several of the beams for the two structures in question. We accordingly list in Table 3 the maximum calculated intensities reached by some of the beams, in the 1$\bar{1}$0 pattern, for material up to 52 nm in thickness both at the Laue orientation and at the Bragg condition for the 001 and 110 orientations. The calculated values can only be used qualitatively since the diffraction pattern was obtained from a region of variable thickness. However, it may be noted from Table 3 that the modified structure gives a greater increase in intensity of the 001 beam at the Bragg condition than does the unmodified structure while the edges of the 001 discs near to the Bragg condition in Fig. 6(*b*) indicate relatively strong diffraction at this orientation.

It would appear that the balance of the indirect evidence given strongly suggests that the atoms at the E sites lie in staggered columns so that at least the local, if not the averaged, structure is $P4_2nm$–C_{4v}^4 rather than $P4_2/mnm$–D_{4h}^{14}.

There are several reasons why the modifications to

the structure should be more readily observable by electron than by X-ray diffraction. Most of these reasons are concerned with specimen preparation. The difficulty of obtaining crystals of suitable size and shape for X-ray studies is mentioned in all articles on the σ phase; for example, Bergman & Shoemaker (1954) used a crystal with dimensions of approximately 0·1 mm. There is also a strong possibility of large-scale faulting in the crystal (see §5). In electron diffraction, size is not a problem (the μm grain size of σ in the material used for this study is of no consequence when using beam probes of the order of 20 to 50 nm). Furthermore, it is a simple matter to find an unfaulted area of σ crystal. However, the complete extent of the structure modification cannot be exactly specified because of the uncertainties in the scattering factors, Debye–Waller factors and the degree of absorption used in the dynamical calculations. In the above calculations, Doyle & Turner (1968) scattering factors were used and the Debye–Waller factors were taken from *International Tables for X-ray Crystallography* (1962).

Examination of the reciprocal-space phase grating (Cowley & Moodie, 1957) used in the dynamical calculations for the system may be used to determine the most likely ordering scheme. For the intensity of a beam to be small at the on-zone orientation the value of the corresponding component of the phase grating must be small. The real and imaginary parts of the 200 and 210 components of the phase grating for the various ordering schemes for both modified and unmodified structures are shown in Fig. 12. The phase grating is for a crystal one unit-cell thick and for 100 kV electrons. The effect of the modification on the structure is to reduce the real part of the amplitude considerably while the ordering scheme affects the imaginary part. The two ordering schemes which give the lowest components in the phase grating are OR5 and OR6.* The first of these schemes is that expected from an overview of all σ phases. The second is not proposed by other authors and is based on the ordering of Fe and Cr atoms in such a way that (210) and (200) planes have the largest possible variations in potential across them. As the stoichiometry of $(Fe–Cr)_\sigma$ is approximately Fe_8Cr_7 there is little difference between the two systems when the mixed sites are occupied randomly. Thus the ordering in $(Fe–Cr)_\sigma$ would appear to be essentially the same as that predicted by a study of all σ phases in general and not that proposed by Bergman & Shoemaker (1954) or Kasper (1956).

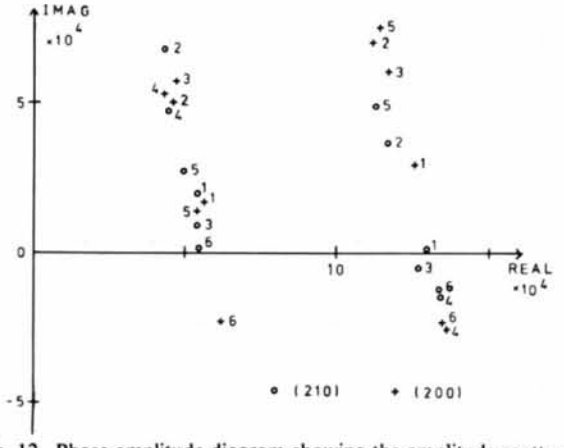

Fig. 12. Phase-amplitude diagram showing the amplitude scattered by one unit cell for the different ordering schemes of Table 2 (1 to 6) for the [200] and [210] beam directions and for a σ structure with and without E-site modification. Note that the group with low real part are for the modified E-site structure. It should also be realized that a contribution in the negative imaginary direction represents scattering with a negative real kinematic structure factor.

Hall & Algie (1966) cite the work of Dickins, Douglas & Taylor (1956) who refined the $(Co–Cr)_\sigma$ structure assuming the β-uranium structure as a starting point and gained a final structure with the E-sited atoms lying in straight columns. However, as is pointed out by Hall & Algie, the structure factors used were derived from a weighted average of the scattering factors of Co and Cr. In other words a solid solution

* The completely mixed structure is dismissed because of the overwhelming evidence of atomic ordering in the σ-phase structure.

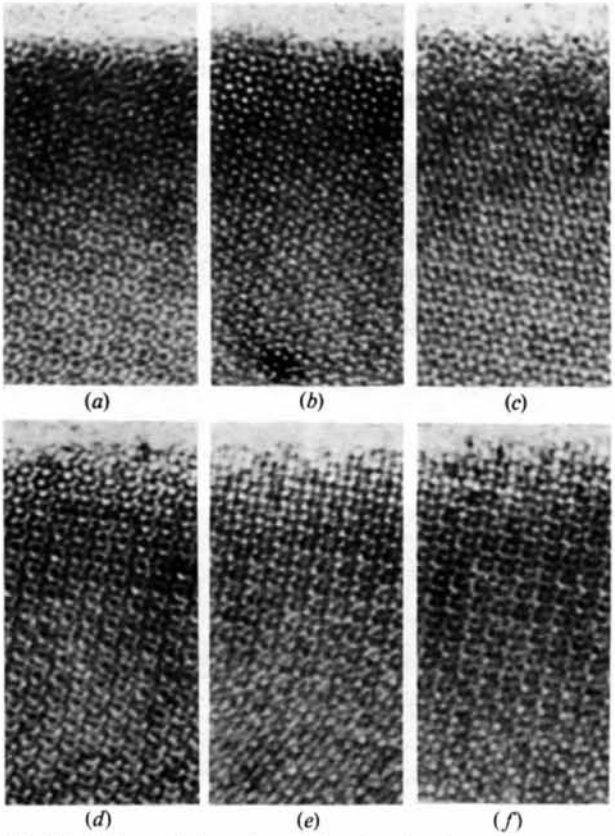

Fig. 13. High-resolution through-focal series from a σ-particle orientated to the 001 zone. Note the characteristic double-diamond pattern in the images at around Scherzer defocus.

was assumed. In a solid solution the modified structure has no kinematical intensity in either the 200 or 210 type reflections and so any intensity found in these beams must be accounted for by moving the *E*-sited atoms back to the original positions.

It is worthwhile to examine the extent to which high-resolution techniques can give more information on the $(Fe–Cr)_\sigma$ structure. Fig. 13 shows a through-focal series of high-resolution images of $(Fe–Cr)_\sigma$. The predominant feature of the images is the double-diamond pattern of spots due to contributions from the 200 and 210 type reflections and also from interaction between the 140 and 330 type reflections (O'Keefe, Self, Southwick & Stobbs, 1980; Ishimasa, Kitano & Komura, 1981*a*, *b*). The computed lattice images (Fig. 14) are in good general agreement with those of Fig. 13. Unfortunately, however, simulated images show that the resolution required to resolve the atoms at say the *C* and *D* sites or similarly spaced sites (let alone the staggering in the *E* sites) is beyond the capability of current high-resolution electron microscopes.

The experimental images show a narrow band of strong contrast around the edge of the specimen. From the thickness profiles of Figs. 9 and 11 this is attributable to the intensity of the 200 and 210 beams in the first 10 nm of crystal thickness. This emphasizes an important generalization which can be made from the computed profiles. In all models examined the thickness fringes were insensitive to the model until the crystal was thicker than 10 nm, *i.e.* thicker than one extinction distance. Hence, if subtle differences in structure are to be distinguished by high-resolution electron microscopy it would be necessary to make careful comparisons of the *intensities* in images and simulations from the thicker regions of the crystal where the differences have significantly modified the diffracted intensities. This means that thickness-dependent properties such as absorption would also need to be suitably accounted for in any image simulation to an accuracy which is not currently possible. In the case of $(Fe–Cr)_\sigma$ the images from the thicker regions are of fairly low contrast because of the form of the zone-axis pattern. A feature of σ-phase images at 001 in thin regions is that they show more contrast at higher convergences because this allows more 200 and 210 intensity to contribute to the image.

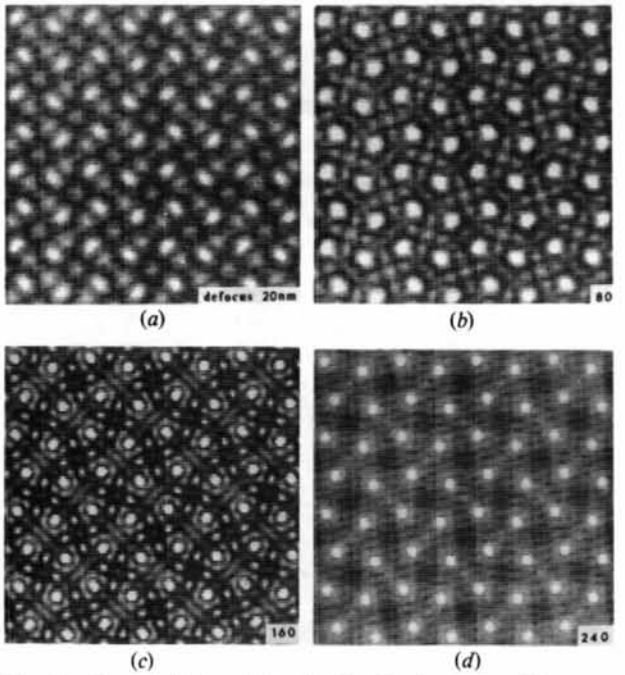

(*a*) (*b*) (*c*) (*d*)

Fig. 14. Computed through-focal series showing reasonable agreement with the experimental images of Fig. 13. C_s and C_c as for Fig. 13.

5. Faults in the σ phase

Frank & Kasper (1959) rationalized the σ structure in terms of the close packing of spheres of slightly different radius. At the same time they realized that the structure would support a series of faults on (100) type planes and indeed were able to postulate new structures by arranging these faults in specific orders. They called these faults 'sequence faults' and pointed out that they did not change coordination numbers of nearest-neighbour distances. Consequently such faults are of low energy. It is worthwhile stressing that these faults are not like stacking faults in that, unlike the latter, they cannot be created by shear and so do not provide a mechanism for slip. Similarly there can be no slip on (001) planes because the atoms at the *E* sites (being at positions $Z = \pm\frac{1}{4}$) lock these planes. The locking of the *E*-sited atoms is often given as a reason for the brittleness of the σ phase. Marcinkowski & Miller (1962) studied sequence faults using TEM and assigned an *f* notation to the six basic sequence faults. This notation will be adopted in this paper.

Several views of faults in the $(Fe–Cr)_\sigma$ structure are given in Fig. 15. Faults are also visible in Figs. 2 and 3. It can be seen that the faults form quite complicated tracks in the σ phase with planar faults mixing freely with faults which are not related to any low-index plane.

Marcinkowski & Miller suggested a mechanism by which faults segment into sequence and non-sequence faults thus reducing the fault energy. As the sequence faults cannot be formed by shear they must be formed by a diffusional growth mechanism. In the alloy used in this study the faults can be formed during the dissolution and entrapment of ferrite by the mechanism suggested in §3. When a piece of entrapped α completely dissolves it is likely to leave dislocations emanating from it pinned at the point where the α finally disappears. This is probably the origin of the

defects seen, for example, at *A* in Fig. 15(*c*). Similarly, any fault involving a component of displacement in the [001] direction will act to stop the growth of sequence faults.

Lattice fringes can be used to specify the type of fault to some degree (Southwick & Stobbs, 1980). Fig. 15(*d*) is an enlarged image of the region of faults marked *b* in Fig. 15(*c*) and shows 100 type fringes. The parallel faults can be seen to lie along (100) planes and have a displacement component of $\frac{1}{2}[100]$ and thus are of the type $f_1^{\ddagger}$ or $f_2^{\ddagger}$. Fig. 16 also shows a fault on (100) planes. By equating the bright dots with the *E* sites (*cf.* §4, O'Keefe *et al.*, 1980; Ishimasa *et al.*, 1981*a*) the fault is characterizable as two f_1^{-} sequence faults side by side as shown by Marcinkowski & Miller (1962, Fig. 4).

One of the faults in Fig. 15(*c*) runs between two heavily dislocated regions (*A* and *a*). The fault is made up of three linear and two curved sections. The shape of the curved faults suggests that they are sweeping through the crystal converting to sequence faults at one end whilst remaining pinned at the other. This is evidence that there are few planes other than (100) type which will support planar faults.

However, the central section of the fault running from *A* to *a* in Fig. 15(*c*) is a planar fault at 45° to the (100) planes. Several of these faults may be seen throughout Fig. 15(*c*). Fig. 17 shows that these faults, which have also been observed by Ishimasa *et al.*

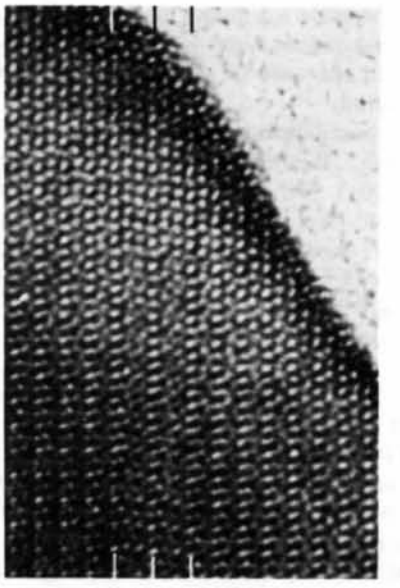

Fig. 16. Lattice image of a double f_1^{-} sequence fault as marked.

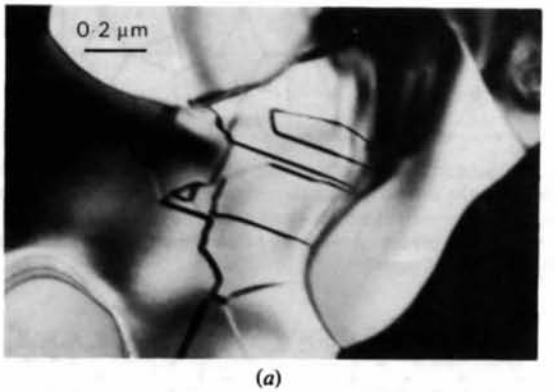

(*a*)

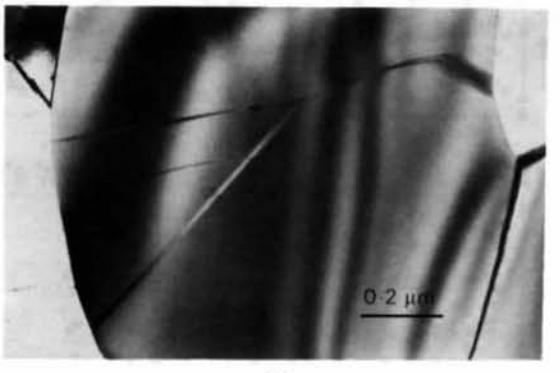

(*b*)

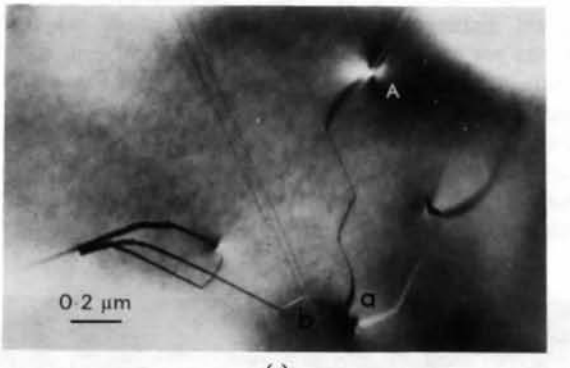

(*c*)

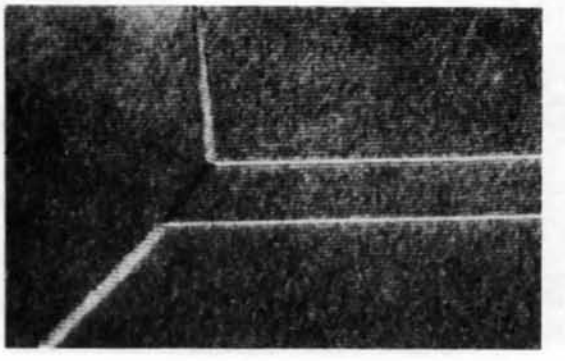

(*d*)

Fig. 15. Typical faulted structures in $(Fe–Cr)_\alpha$. (*d*) shows 100 lattice fringes and is an enlargement of area *b* in (*c*). Given the constancy of the contrast across a fault the fringes may be used to measure the 100 component of the displacement across the faults.

(1981*b*), lie on (110) planes and by measuring the lattice fringes they can be assigned a displacement vector of approximately $\frac{1}{3}[1\bar{1}0]$ (actually $0{\cdot}34 \pm 0{\cdot}03[1\bar{1}0]$). While planar faults of this type have not until recently been discussed, Holden (1952) showed that the (110) plane is a possible slip plane in β-uranium and pointed out that these planes were the only true flat ones in the structure. In the case of β-uranium slip occurs in the [001] direction.

Several possibilities exist for the generation of a $\frac{1}{3}(1\bar{1}0)$ fault. Examination of the hexagonal nets forming (001) planes reveals that a translation of $\frac{1}{3}[110]$ would be a perfect lattice vector for one of the nets if the *E*-sited atoms lay in the $z = 0$ and $\frac{1}{2}$ planes. The other net has a perfect lattice vector of $\frac{2}{3}[110]$. Thus an $\frac{11}{30}(110)$ fault can be generated by a shear of the structure in a ⟨110⟩ direction followed by some relaxation at a few *C*, *D* and *E* sites along the fault. Similarly the fault may be formed by the removal of two (110) planes and relaxation at some *B* and *E* sites along the fault.

There are three types of (110) plane in the σ-phase structure but these may be reduced to two main types. These are shown in Fig. 18 and are labelled *A* and *B*. The σ structure is specified by the stacking sequence

$$A^{+}B^{+}B_{m}ABB_{m}^{+}A^{+}$$

as shown in Fig. 19(*a*). The + indicates a shift by $\frac{1}{2}$ a repeat distance along the $[\bar{1}10]$ direction. As the *B* planes are not strictly flat (*C* and *D* sites being slightly above and below the plane as indicated in Fig. 18) it is necessary to distinguish between the mirror image of *B*-type planes as indicated by the subscript *m*. By varying the above stacking sequence several (110) faults may be described. As stated above a fault can be generated by a shear of approximately $\frac{1}{3}[\bar{1}10]$ giving the two types of fault as shown in Figs. 19(*b*) and (*c*). Of these the one in Fig. 19(*b*) would seem to be preferable in that the other has several atoms (joined by a line in the figure) which are unrealistically close together.

The other class of fault can be generated by removal of two layers from the sequence giving the two types of fault shown in Figs. 19(*d*) and (*e*). The first is formed by the removal of two *B* layers and is rather an open fault. For this reason it would be more favourable than the second type (Fig. 19*e*) which again has several atoms very close together along the fault. Indeed, as these atoms lie in the same plane and are so close together it would not be unreasonable to suggest a still further (110) fault, perhaps particularly relevant for non-stoichiometric σ, with these atom positions amalgamated as shown in Fig. 19(*f*). It should be noted that in all faults one tiling net is left undistorted and the other is only slightly distorted.

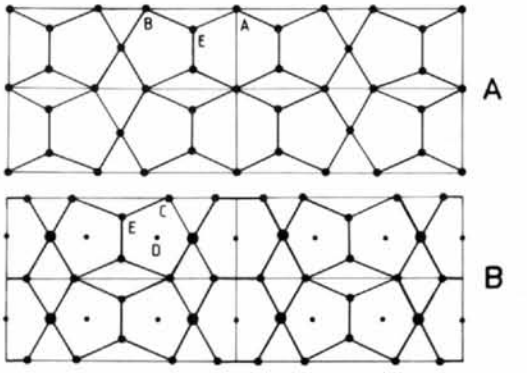

Fig. 18. Schematics of the two characteristic sections which describe the σ structure as viewed in a $[1\bar{1}0]$ direction. The large dots in *B* represent atoms positioned above the page whilst the small dots represent those lying below the page. The site labelling is as in Fig. 5.

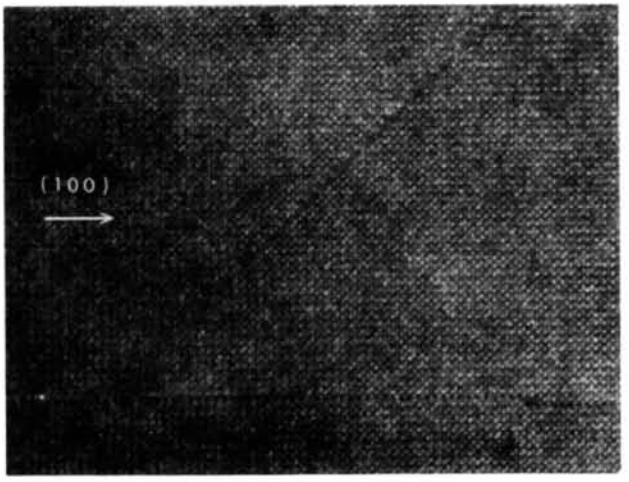

Fig. 17. Lattice image of a fault lying on a (110) plane. The displacement across the fault is $\frac{1}{3}(110)$ as measured by the lattice fringes.

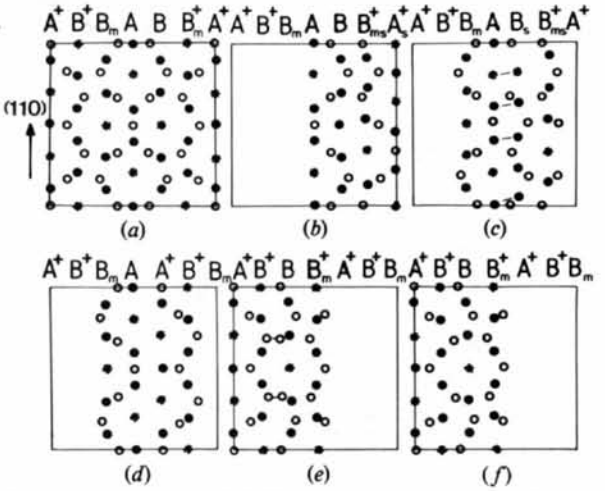

Fig. 19. Arrangements of (110) planes which could give rise to a $\frac{1}{3}(1\bar{1}0)$ type fault. (*a*) shows the unfaulted structure.

A third, though presumably unfavourable, way exists of producing faults in the σ structure. If the Kagomé tiling nets were to change character (*i.e.* from l.h. to r.h. and *vice versa*) along a $\langle 110 \rangle$ direction then the resulting fault would be of $\frac{1}{6}\langle 223 \rangle$ type. The mismatch between the nets can be taken up by using subunits of another of the tessellations described by Frank & Kasper (1959). In particular, units of the pentagon strips used in the *P*-phase structure can facilitate this change. The fault in Fig. 17 forms an intersection with two (100) sequence faults which do not have a component (other than a whole lattice vector) in the *Z* direction. Thus the (110) fault cannot have a component of $\frac{1}{2}(001)$ otherwise the intersection would show considerable strain. As it is, no two sequence faults can combine to form a displacement component of $\frac{1}{3}(110)$ and so a small amount of relaxation is required at the intersection. Careful examination of Fig. 17 shows that the mismatch is taken up mostly by the (110) fault.

6. Conclusions and summary

Three aspects of the $(Fe–Cr)_\sigma$ phase have been considered in this paper, firstly its growth in a particular steel alloy, secondly its structure and thirdly the form of the defects the phase tends to contain.

In its growth from the steel, it has been demonstrated that (*a*) σ-phase particles grow rapidly once nucleation has taken place, (*b*) nucleation can occur both on defects and boundaries in the ferrite and, with a given orientation relationship, at α/γ boundaries with subsequent growth into the ferrite, (*c*) it is the tendency for nucleation and growth in the first of the above manners which leads both to a honeycomb structure of σ-phase particles with entrapped ferrite and austenite, and to the introduction of sequence and other faults in σ as entrapment is completed.

It has been demonstrated by an examination and analysis of its electron scattering behaviour that the $(Fe–Cr)_\sigma$ structure probably has space group $P4_2nm$–C_{4v}^4. This space group has slightly less symmetry than the group $P4_2/mnm$–D_{4h}^{14} which is the space group previously accepted for the σ-phase structure as based on X-ray diffraction evidence. The reduction in symmetry suggested is considered to arise because atoms lying in the $Z = \frac{1}{4}$ and $\frac{3}{4}$ sites are laterally staggered and hence remain in the hexagonal Kagomé net positions, rather than lying in straight vertical columns. It was further demonstrated that the contrast of high-resolution images of approximately weak-phase nature (*i.e.* thin-crystal images) is too insensitive to the change in atomic displacement to distinguish between models. Any attempt by high-resolution imaging to distinguish between the models could only be done by full comparison of simulated and experimental images for much thicker regions of crystal than are normally required for such a structural analysis. This would necessarily require a better understanding of the extent to which inelastic scattering is important than is currently available. We suggest that if suitable crystals can be found neutron diffraction work might provide further evidence for the structure we propose.

While the generally accepted nature of the displacements at (001) sequence faults was further confirmed, a new fault with a displacement of approximately $\frac{1}{3}\langle 110 \rangle$ was characterized and modelled. It was shown that this fault could grow by either shear or some form of diffusional growth mechanism.

We are grateful to the SRC for financial support and to Professor Honeycombe for provision of laboratory facilities. Our thanks go to Dr P. D. Southwick for his helpful advice on material and specimen preparations. The authors also acknowledge Cambridge Fine Instruments for supplying a double-tilt holder for the 0·7 C_s JEOL pole piece of the JEOL 120CX used for the high-resolution work.

References

BERGMAN, G. & SHOEMAKER, D. P. (1954). *Acta Cryst.* **7**, 857–865.
COWLEY, J. M. & MOODIE, A. F. (1957). *Acta Cryst.* **10**, 609–619.
DICKINS, G. J., DOUGLAS, A. M. B. & TAYLOR, W. H. (1956). *Acta Cryst.* **9**, 297–303.
DOYLE, P. A. & TURNER, P. S. (1968). *Acta Cryst.* **A24**, 390–397.
DUWEZ, P. & BAEN, S. R. (1951). *Symposium on the Nature, Occurrence and Effects of the σ Phase. Am. Soc. Test. Mater. Spec. Tech. Publ.* np 110, p. 48. Philadelphia, PA: American Society for Testing Materials.
FRANK, F. C. & KASPER, J. S. (1959). *Acta Cryst.* **12**, 483–499.
GJØNNES, J. & MOODIE, A. F. (1965). *Acta Cryst.* **19**, 65–67.
HALL, E. O. & ALGIE, J. H. (1966). *Metall. Rev.* **11**, 61–88.
HOLDEN, A. N. (1952). *Acta Cryst.* **5**, 182–184.
International Tables for X-ray Crystallography (1962). Vol. III. Birmingham: Kynoch Press.
ISHIMASA, T., KITANO, T. & KOMURA, Y. (1981*a*). *J. Solid State Chem.* **36**, 74–80.
ISHIMASA, T., KITANO, T. & KOMURA, Y. (1981*b*). *Phys. Status Solidi A*, **66**, 703–715.
KASPER, J. S. (1956). *Theory of Alloy Phases*, p. 264. Cleveland, Ohio: ASM.
LEWIS, M. H. (1966). *Acta Cryst.* **14**, 1421–1428.
LYNCH, D. (1971). *Acta Cryst.* **A27**, 399–407.
MARCINKOWSKI, M. J. & MILLER, P. S. (1962). *Philos. Mag.* **7**, 1025–1059.
O'KEEFE, M. A., SELF, P. G., SOUTHWICK, P. D. & STOBBS, W. M. (1980). In *Electron Microscopy* 1980. Proceedings of EUREM 80, edited by P. BREDERON & G. BOOM, p. 264. Seventh European Congress on Electron Microscopy Foundation, Leiden.
SOUTHWICK, P. D. (1978). *Microstructural Studies on a Duplex Stainless Steel.* PhD Thesis, Univ. of Cambridge, England.
SOUTHWICK, P. D. & HONEYCOMBE, R. W. K. (1980). *Met. Sci.* **14**, 253–261.
SOUTHWICK, P. D. & STOBBS, W. M. (1980). *J. Microsc.* **119**, 169.